

# Lattice O–O ligands triggered Fe activation for superior oxygen-evolving electrocatalysis

**Liming Zhang** (✉ [zhanglm@fudan.edu.cn](mailto:zhanglm@fudan.edu.cn))

Fudan University <https://orcid.org/0000-0001-6795-3381>

**Guoshuai Shi**

<https://orcid.org/0000-0001-9588-3368>

**Jili Li**

Fudan University

**Chunlei Yang**

Fudan University

**Huoliang Gu**

Fudan University

**Haonan Tong**

Fudan University

**Siwen Zhao**

Fudan University

**Chenyuan Zhu**

Fudan University

**Yuluo Shen**

Fudan University

**Jing Wu**

Fudan University

**Jiong Li**

Shanghai Advanced Research Institute, CAS <https://orcid.org/0000-0001-6826-9987>

**Shuo Zhang**

Shanghai Synchrotron Radiation Facility, Shanghai Advanced Research Institute, Chinese Academy of Sciences

**Jueli Shi**

Xiamen University

**Kelvin H.L. Zhang**

Xiamen University

**Yefei Li**

Fudan University

**Zhipan Liu**

Fudan University <https://orcid.org/0000-0002-2906-5217>

---

## Physical Sciences - Article

**Keywords:**

**Posted Date:** May 9th, 2022

**DOI:** <https://doi.org/10.21203/rs.3.rs-1524224/v1>

**License:**  This work is licensed under a Creative Commons Attribution 4.0 International License.

[Read Full License](#)

**Additional Declarations:** There is **NO** Competing Interest.

---

# Abstract

Understanding the structural dynamics of ligands and its interplay with the turnover rate of catalytic centers under reaction conditions are challenging but crucial regarding catalyst design. Here, an *in-situ* phase conversion of Ni-Fe hydroxide to a stable superoxo-hydroxide, with the formation of lattice O–O ( $O_{\text{latt}}-O_{\text{latt}}$ ) ligands, was unveiled via operando  $^{18}\text{O}$ -labeling spectroelectrochemistry and machine-learning global optimization. By correlating the intrinsic activity of Fe with the ability of  $O_{\text{latt}}-O_{\text{latt}}$  formation in a series of Fe-incorporated transition-metal oxides/hydroxides, we disclose an  $O_{\text{latt}}-O_{\text{latt}}$  triggered Fe activation for oxygen-evolving electrocatalysis, which is further proved by first-principles calculations. The oxygen production follows an adsorbate evolution mechanism and the fast kinetics is attributed to diminished Fe–OH bonds in the presence of  $O_{\text{latt}}-O_{\text{latt}}$ . This work guides the rational design of high-performance Fe-incorporated electrocatalysts, and highlights the paramount role of ligands dynamic restructuring in awakening catalytic centers.

# Full Text

Electrochemical reactions involving oxygen molecules, such as those occurring at water electrolyzers, fuel cells and metal-air batteries, are ubiquitous in energy conversion and storage technologies<sup>1–3</sup>. A particularly important scenario of oxygen electrochemical reactions is one that oxidizes water to oxygen molecules, the sluggish kinetics of which is among the most serious bottlenecks that restrict the power-to-gas efficiency of water electrolyzers<sup>4</sup>. Such a four proton-electron transfer process is significantly more complex and less understood than the electrochemical proton reduction at cathode, where only two electron transferring are needed to produce one hydrogen molecule.

Non-precious transition-metal (TM) oxides with perovskite<sup>5–6</sup>/spinel<sup>7</sup> structures and TM hydroxides<sup>8–10</sup> with layered structures, typically based on Mn, Fe, Co and Ni, are extensively studied as electrocatalysts and demonstrate remarkable performances towards oxygen evolution reaction (OER). The redox behavior of TM cations suggests that they are the redox partners to molecular oxygen ( $\text{O}_2$ ) during electrochemical reactions<sup>11–14</sup>. Several OER activity descriptors solely based on characters of the metal core, such as OH– $\text{M}^{2+\delta}$  bond strength<sup>8</sup>,  $e_g$  orbital occupancy<sup>6</sup> and M–O covalency<sup>7,15</sup> have been proposed. However, more evidences on traditional thermo-and bio-catalysis suggest that for a particular reaction, the ligands environment surrounding catalytic centers is crucial for the exquisite catalytic specificity. A typical manifestation of this phenomenon is that, as shown in enzyme catalysis, the active center can only achieve a superior catalytic specificity and turnover within a particular bonding environment<sup>16,17</sup>. Towards this end, the attribution of active sites solely to metal centers without considering the impact from ligands microenvironment may not be sufficient for OER electrocatalysis. Although understanding the coordination of active center with ligands is crucial to establish the accurate structure-performance correlation, it remains a grand challenge in heterogeneous electrocatalysis, in particular when complicated ligands restructuring associates with catalysis under working conditions. In TM oxides/hydroxides, the chemical states of oxygen ligands tend to evolve gradually under an external bias

in OER<sup>18–22</sup>, and the restructuring of oxygen ligands and its complex interplay with OER kinetics remain ambiguous. The lack of such understanding would heavily impede the rational design of high-performance OER electrocatalysts.

A model material for investigating the influence of ligands is layered nickel-iron hydroxide ( $\text{Ni}_{1-x}\text{Fe}_x\text{O}_y\text{H}_z$ ), which has been considered a most excellent candidate OER electrocatalyst in alkaline for decades<sup>4,9,23,24</sup>. Each layer of  $\text{Ni}_{1-x}\text{Fe}_x\text{O}_y\text{H}_z$  consists of edge-sharing  $\text{NiO}_6$  and  $\text{FeO}_6$  octahedra, such that the neighboring metal sites share two bridging lattice oxygen ions. It has been well documented that the primitive nickel hydroxide has a poor catalytic performance, whereas a certain content of Fe doping (< 40%) can increase the OER activity by more than 100-fold<sup>25,26</sup>. The origin of enhanced OER performance from Fe incorporation was under intense debate for over 30 years<sup>9,10,12,23–32</sup>. In this work, combining theories and experiments, we unveiled the key role of lattice O–O ( $\text{O}_{\text{latt}}-\text{O}_{\text{latt}}$ ) ligands in Fe activation for superior OER. Machine-learning global optimization and <sup>18</sup>O-labeling *operando* spectroelectrochemistry identified an *in-situ* formation of Ni-Fe *superoxo*-hydroxide with unique  $\text{O}_{\text{latt}}-\text{O}_{\text{latt}}$ , which consequently triggers the activation of Fe sites. We further discovered that the turn-over-frequency of Fe ( $\text{TOF}_{\text{Fe}}$ ) positively correlates with the ease of lattice oxygen coupling in a series of Fe-incorporated oxides/hydroxides with different geometric and electronic structures *e.g.*, hydroxide-type  $\text{M}_{1-x}\text{Fe}_x\text{O}_y\text{H}_z$  (M= Mn, Fe, Co, Ni and Cu), perovskite-type  $\text{LaNi}_{1-x}\text{Fe}_x\text{O}_3$  and spinel-type  $\text{NiFe}_2\text{O}_4$ . Density Functional Theory (DFT) calculations revealed that the  $\text{O}_{\text{latt}}-\text{O}_{\text{latt}}$  formation diminishes Fe–OH bonds and thus accelerates the turnover rate at Fe sites. Our results demonstrate a brand-new Fe activation mechanism for OER, and setup a paradigm to show the importance of *operando* ligands restructuring in electrocatalysis at an atomic scale.

**$\text{O}_{\text{latt}}-\text{O}_{\text{latt}}$  formation under OER.** The phase conversion of  $\text{Ni}_{1-x}\text{Fe}_x\text{O}_y\text{H}_z$  to *superoxo*-hydroxide with  $\text{O}_{\text{latt}}-\text{O}_{\text{latt}}$  ligands was first identified using the neural network (NN) potential in combination with stochastic surface walking (SSW) global optimization (See details in Methods). Fig. 1a shows the formation energy of bulk  $\text{Ni}_{0.75}\text{Fe}_{0.25}\text{O}_x(\text{OO})_n\text{H}_y\cdot z\text{H}_2\text{O}$  per formula unit (f.u.) with different  $\text{O}_{\text{latt}}-\text{O}_{\text{latt}}$  contents at 1.53 V versus reversible hydrogen electrode ( $V_{\text{RHE}}$ ), where  $\text{Ni}_{0.75}\text{Fe}_{0.25}\text{O}_2\text{H}$  is the reference zero. More SSW-NN results regarding metastable  $\text{Ni}_{0.75}\text{Fe}_{0.25}\text{O}_x(\text{OO})_n\text{H}_y\cdot z\text{H}_2\text{O}$  phases with varied numbers of protons and  $\text{H}_2\text{O}$  molecules are shown in Supplementary Table 1. Each composition was explored  $10^4$  minima structures to search for the most stable structure of  $\text{Ni}_{0.75}\text{Fe}_{0.25}\text{O}_x(\text{OO})_n\text{H}_y\cdot z\text{H}_2\text{O}$  under OER. The global minimum (GM) structure,  $\text{Ni}_{0.75}\text{Fe}_{0.25}\text{O}(\text{OO})\text{H}_{0.5}\cdot\text{H}_2\text{O}$ , consist of alternated  $\text{NiO}(\text{OO})\text{H}_{0.75}$  and  $\text{Ni}_{0.5}\text{Fe}_{0.5}\text{O}(\text{OO})\text{H}_{0.25}$  sheets and interlayer water molecules, is highlighted in Fig. 1a. Notably, the GM structure exhibits a large amount of  $\text{O}_{\text{latt}}-\text{O}_{\text{latt}}$ . In addition, Fe is more prone to segregate out rather than uniformly disperse in catalyst, which is in line with recent observations in OER experiments<sup>33</sup>. To further verify the stability of  $\text{O}_{\text{latt}}-\text{O}_{\text{latt}}$  on surface, we performed SSW-NN global optimization on  $\text{Ni}_{0.75}\text{Fe}_{0.25}\text{O}(\text{OO})\text{H}_{0.5}\cdot\text{H}_2\text{O}$  (010) surface, and our results show no reconstruction occurs (after searching  $10^4$  minima). Furthermore, the free energy change for desorption of  $\text{O}_{\text{latt}}-\text{O}_{\text{latt}}$  from lattice to a gas

O<sub>2</sub> molecule is +0.08 eV, suggesting O<sub>latt</sub>-O<sub>latt</sub> ligands are stable on surface under electrochemical conditions.

In experiment, we confirmed the formation of O<sub>latt</sub>-O<sub>latt</sub> ligands under working conditions. We applied *operando* Raman spectroscopy in combination with <sup>18</sup>O-labeling experiments to evidence the lattice oxygen coupling. Ni<sub>0.72</sub>Fe<sub>0.28</sub><sup>16</sup>O<sub>y</sub>H<sub>z</sub> (see details in Methods for synthesis) was measured in a 0.1 M solution of Fe-free K<sup>16</sup>OH, and Raman signals were barely observed at an open circuit potential (OCP). When applying a bias at 1.65 V<sub>RHE</sub>, Raman spectra clearly showed several new features (Fig. 1b). The peaks at 480 cm<sup>-1</sup> and 560 cm<sup>-1</sup> were assigned to E<sub>g</sub> bending and A<sub>1g</sub> stretching modes of Ni-O<sup>30,34</sup>, respectively, and the broad peak at ~1045 cm<sup>-1</sup> was ascribed to O-O bond<sup>30,34</sup>. According to previous reports<sup>35,36</sup>, the O-O stretching frequency at 1045 cm<sup>-1</sup> indicates a bridging O-O with a bond length of ~1.36 Å, which is consistent with the O-O structure in our SSW-NN calculation (Fig. 1a and Supplementary Fig. 1). More O-O structures and corresponding vibrational frequencies were summarized in Supplementary Table 2. To identify the oxygen sources of O-O, we first labeled the <sup>18</sup>O-KOH electrolyte while keeping <sup>16</sup>O in catalyst. It was observed that the vibration frequencies of both Ni-O and O-O in <sup>18</sup>O-KOH are almost identical to those observed in <sup>16</sup>O-KOH without shifting. Next, we labeled the Ni<sub>0.72</sub>Fe<sub>0.28</sub><sup>18</sup>O<sub>y</sub>H<sub>z</sub> catalyst (see Supplementary Note 1) and <sup>18</sup>O-KOH electrolyte, and observed that the signals of both Ni-O and O-O obviously red-shift in relative to those of Ni<sub>0.72</sub>Fe<sub>0.28</sub><sup>16</sup>O<sub>y</sub>H<sub>z</sub>, with the center positions shifting by 20 and 40 cm<sup>-1</sup>, respectively. We further used Ni<sub>0.72</sub>Fe<sub>0.28</sub><sup>18</sup>O<sub>y</sub>H<sub>z</sub> catalyst and <sup>16</sup>O-KOH electrolyte, which demonstrated barely shifted Ni-O and O-O signals comparing with those observed on Ni<sub>0.72</sub>Fe<sub>0.28</sub><sup>18</sup>O<sub>y</sub>H<sub>z</sub> in <sup>18</sup>O-KOH. These results convinced that the oxygen in O-O ligands is from the lattice. In chronoamperometry measurements under static potentials, the Raman signal of O<sub>latt</sub>-O<sub>latt</sub> is stable without peak shifting, meaning that the oxygen atoms in O<sub>latt</sub>-O<sub>latt</sub> are stable without exchanging with the electrolyte (Supplementary Fig. 2). Our results strongly suggest that (1) the O-O bond forms via lattice oxygen coupling in catalyst rather than external OH<sup>-</sup>/H<sub>2</sub>O incorporation from electrolyte; (2) the long-lived O<sub>latt</sub>-O<sub>latt</sub> species are stable and hardly to release as O<sub>2</sub> molecules.

Beyond Raman, we further applied *operando* X-ray absorption spectroscopy (XAS) to identify the local coordination restructuring of Ni<sub>0.63</sub>Fe<sub>0.37</sub>O<sub>y</sub>H<sub>z</sub>. As for Fe, although the position of Fe K-edge remained unchanged, the intensity of the white-line peak gradually declined as the positive bias increasing (Supplementary Fig. 3), indicative of a symmetry broken of FeO<sub>6</sub> octahedras.<sup>27,37</sup> Moreover, the Fourier-transformed k<sup>3</sup>-weighted extended X-ray absorption fine structure (FT-EXAFS) with fitting parameters (Fig. 1c and Supplementary Table 3) and the wavelet transform (WT) plot (Supplementary Fig. 4) further confirm the destroyed local symmetry of Fe under OER. We also observed a similar phenomenon of Ni under a positive bias, and the results were summarized in Supplementary Table 3, Figs. 5 and 6. The distorted FeO<sub>6</sub> and NiO<sub>6</sub> octahedras can be ascribed to the restructuring of oxygen ligands nearby, which is resulted from the lattice oxygen coupling in Ni-Fe superoxo-hydroxide, as confirmed by SSW-NN calculation and <sup>18</sup>O-labeling Raman spectroscopy.

**$O_{\text{latt}}-O_{\text{latt}}$  triggered Fe activation in TM hydroxide.** To investigate the impact of  $O_{\text{latt}}-O_{\text{latt}}$  on electrocatalysis, we first study the formation of  $O_{\text{latt}}-O_{\text{latt}}$  ligands from a theoretical perspective. To form an  $O_{\text{latt}}-O_{\text{latt}}$ , two  $M^{n+}-O^{2-}$  pairs need to firstly discharge to  $M^{(n-1)+}-O^-$ , and then, two  $O^-$  anions couple together to generate one  $O_{\text{latt}}-O_{\text{latt}}$ , leaving an oxygen vacancy, which will be subsequently occupied by  $OH^-$  in an alkaline electrolyte (Supplementary Fig. 7). Because the valence band maximum (VBM) and conduction band minimum (CBM) typically arise from O 2p and M 3d orbitals, respectively (shown in Fig. 2a), it is reasonable to expect that the gap between O 2p and M 3d, denoted as  $E_G(O, M)$ , is proportional to the energetic cost of discharge of  $M^{n+}-O^{2-} \rightarrow M^{(n-1)+}-O^-$ , if the following  $O^- - O^-$  coupling is accessible. Notably,  $O^- - O^-$  coupling is also significantly influenced by the geometric structure, which will be discussed later. To this end,  $E_G(O, M)$  calculated by DFT can be regarded as a parameter to evaluate the ease of  $O_{\text{latt}}-O_{\text{latt}}$  formation, in particular when the geometric environment is similar.

We correlate  $E_G(O, M)$  with the intrinsic activities of Fe-incorporated TM hydroxides. Fig. 2b shows the projected density of states (PDOS) of  $M_{0.75}Fe_{0.25}O_yH_z$  ( $M = Mn, Fe, Co, Ni$  and  $Cu$ ), which indicates an  $O_{\text{latt}}-O_{\text{latt}}$  formation tendency:  $NiFeO_yH_z > CoFeO_yH_z > CuFeO_yH_z \approx MnFeO_yH_z > FeO_yH_z$ . A series of ultra-thin  $M_{1-x}Fe_xO_yH_z$  were synthesized for electrochemical measurements (see Methods for details), to ensure the full exposure of active sites. The Fe content, determined by inductively coupled plasma optical emission spectrometry (ICP-OES), was controlled within  $25 \pm 3\%$  except  $FeO_yH_z$  ( $x = 0.25 \pm 0.03$ , Supplementary Table 4). For simplicity,  $MFeO_yH_z$  was used to denote the series of hydroxide materials hereinafter. The projected area normalized current densities of  $MFeO_yH_z$  were compared in a 1 M purified KOH solution (Fig. 2c), which unambiguously demonstrates different OER activities.  $NiFeO_yH_z$  and  $CoFeO_yH_z$  show dramatically higher OER current densities comparing with  $CuFeO_yH_z$ ,  $MnFeO_yH_z$  and  $FeO_yH_z$ . We further calculated  $TOF_{Fe}$  of  $MFeO_yH_z$  in Supplementary Fig. 8, according to the OER current at a 300 mV overpotential and number of Fe sites determined by ICP-OES. It was observed that the  $TOF_{Fe}$  of  $NiFeO_yH_z$  and  $CoFeO_yH_z$  are remarkably higher than other counterparts. In particular, the  $TOF_{Fe}$  of  $NiFeO_yH_z$  reached  $0.60 \pm 0.20 \text{ s}^{-1}$ , over 2 orders of magnitudes higher than those of  $CuFeO_yH_z$  and  $MnFeO_yH_z$ , indicating Fe sites in different hydroxides perform very differently, even though they share a similar initial geometric structure and Fe concentration. Importantly, we observed that  $TOF_{Fe}$  increases exponentially with the drop of  $E_G(O, M)$  in layered  $MFeO_yH_z$  (Fig. 2d), which indicates the key role of  $O_{\text{latt}}-O_{\text{latt}}$  ligands for Fe activation. The easier of the catalyst to perform lattice oxygen coupling, the higher  $TOF_{Fe}$  can be expected.

*Operando* Raman measurement was also performed to evidence the correlation between  $O_{\text{latt}}-O_{\text{latt}}$  ligands and Fe catalytic activity. The  $O_{\text{latt}}-O_{\text{latt}}$  signal was barely observed on  $CuFeO_yH_z$ ,  $FeO_yH_z$  and  $MnFeO_yH_z$  under a positive bias (Supplementary Fig. 9), consistent with their poor OER activities. Similar to  $NiFeO_yH_z$ , the signal of  $O_{\text{latt}}-O_{\text{latt}}$  can be identified on  $CoFeO_yH_z$  under OER (Supplementary Fig. 10), which is in-line with the advanced OER performance of  $CoFeO_yH_z$ .

**The universality of  $O_{\text{latt}}-O_{\text{latt}}$  triggered Fe activation.** We further investigated the universal role of  $O_{\text{latt}}-O_{\text{latt}}$  ligands for Fe activation in TM oxides with different geometric structures, including perovskite  $\text{LaNi}_{1-x}\text{Fe}_x\text{O}_3$  and spinel  $\text{NiFe}_2\text{O}_4$ . The PDOS of  $\text{LaNi}_{0.75}\text{Fe}_{0.25}\text{O}_3$  and  $\text{NiFe}_2\text{O}_4$  were calculated in Supplementary Fig. 11, both of which show a lower  $E_{\text{G}}(\text{O}, \text{M})$  than  $\text{Ni}_{0.75}\text{Fe}_{0.25}\text{O}_y\text{H}_z$ . This result indicates the discharge step of  $\text{M}^{n+}-\text{O}^{2-}$  to  $\text{M}^{(n-1)+}-\text{O}^-$  is easier for perovskite  $\text{LaNi}_{0.75}\text{Fe}_{0.25}\text{O}_3$  and spinel  $\text{NiFe}_2\text{O}_4$ . However, unlike hydroxide has a flexible two-dimensional (2D) structure with an open oxygen environment, perovskite and spinel display three-dimensional (3D) rigid structures (Fig. 3a and Supplementary Fig. 12). Therefore, in both cases, the lattice  $\text{O}^- - \text{O}^-$  coupling step (rather than the discharge of  $\text{M}^{n+}-\text{O}^{2-}$ ) limits the dimerization, which is strongly hindered by their rigid geometric structures.

We benchmarked the OER activities of  $\text{Ni}_{1-x}\text{Fe}_x\text{O}_y\text{H}_z$ ,  $\text{LaNi}_{0.75}\text{Fe}_{0.25}\text{O}_3$  and  $\text{NiFe}_2\text{O}_4$  to verify  $O_{\text{latt}}-O_{\text{latt}}$  triggered Fe activation. Both  $\text{LaNi}_{1-x}\text{Fe}_x\text{O}_3$  and  $\text{NiFe}_2\text{O}_4$  were synthesized via modified sol-gel methods<sup>38</sup>, and  $\text{Ni}_{1-x}\text{Fe}_x\text{O}_y\text{H}_z$  were synthesized via a modified hydrothermal procedure<sup>39</sup> (see more details in Methods). The Ni/Fe stoichiometry was determined by ICP-OES (Supplementary Table 5). The long-range crystal structures and local bonding characteristics of three catalysts were confirmed by X-ray diffraction (XRD) and XAS, respectively (Supplementary Figs. 13, 14 and Table 6). Supplementary Fig. 15 shows the CVs of  $\text{Ni}_{0.72}\text{Fe}_{0.28}\text{O}_y\text{H}_z$ ,  $\text{LaNi}_{0.75}\text{Fe}_{0.25}\text{O}_3$  and  $\text{NiFe}_2\text{O}_4$ , evidencing the poor activities of  $\text{LaNi}_{0.75}\text{Fe}_{0.25}\text{O}_3$  and  $\text{NiFe}_2\text{O}_4$  in relative to  $\text{Ni}_{0.72}\text{Fe}_{0.28}\text{O}_y\text{H}_z$ . We further calculated the  $\text{TOF}_{\text{Fe}}$  of three structures (Fig. 3b), assumed all Fe in catalysts, the amount of which were determined by ICP-OES, are active for OER. It is observed that the  $\text{TOF}_{\text{Fe}}$  of  $\text{Ni}_{1-x}\text{Fe}_x\text{O}_y\text{H}_z$  is 2–3 orders of magnitudes higher than those of  $\text{LaNi}_{1-x}\text{Fe}_x\text{O}_3$  and  $\text{NiFe}_2\text{O}_4$ . Meanwhile,  $\text{TOF}_{\text{surface-Fe}}$  was further calculated, which assumes only Fe locating at surface is active (see Supplementary Note 2), to eliminate the influence of surface area on activity. The  $\text{TOF}_{\text{surface-Fe}}$  in Supplementary Fig. 16 further proves the inferior activities of Fe in perovskite and spinel, which can be well explained by the absence of  $O_{\text{latt}}-O_{\text{latt}}$  ligands.

*Operando* Raman and XAS were performed to confirm the lack of  $O_{\text{latt}}-O_{\text{latt}}$  and Fe local restructuring, respectively. As shown in Figs. 3c and d, no O–O feature appears at positive potentials, indicative of the intact oxygen ligands in perovskite and spinel during OER. Similar to Raman results, for both Ni and Fe K-edges, no evolution of XANES and EXAFS were detected in  $\text{LaNi}_{0.61}\text{Fe}_{0.39}\text{O}_3$  and  $\text{NiFe}_2\text{O}_4$  under different positive potentials (Figs. 3e–f, Supplementary Figs. 17–21, Tables 7 and 8), indicative of their stable electronic and local coordination structures of metal centers. These results successfully proved the absence of  $O_{\text{latt}}-O_{\text{latt}}$  ligands in  $\text{LaNi}_{0.61}\text{Fe}_{0.39}\text{O}_3$  and  $\text{NiFe}_2\text{O}_4$ , which can be attributed to the difficult  $\text{O}^- - \text{O}^-$  coupling in such 3D rigid structures. The inferior OER activities of  $\text{LaNi}_{1-x}\text{Fe}_x\text{O}_3$  and  $\text{NiFe}_2\text{O}_4$  further indicate the crucial role of  $O_{\text{latt}}-O_{\text{latt}}$  ligands for Fe activation.

**Mechanistic understanding.** To unveil the  $O_{\text{latt}}-O_{\text{latt}}$  triggered Fe activation mechanism, we calculated OER free energy profiles on exposed Fe sites of  $\text{Ni}_{0.75}\text{Fe}_{0.25}\text{O}_3\text{H}_{0.5}\cdot\text{H}_2\text{O}$  (010) (GM structure). As shown in

Fig. 4a, OER follows an adsorbate evolution mechanism (AEM) on  $\text{Ni}_{0.75}\text{Fe}_{0.25}\text{O}_3\text{H}_{0.5}\cdot\text{H}_2\text{O}$  (010) surface, *i.e.*,  $^*\text{H}_2\text{O} \rightarrow ^*\text{OH} \rightarrow ^*\text{O} \rightarrow ^*\text{OOH} \rightarrow \text{O}_2(\text{g})$ . The AEM process is consistent with previously reported isotope labeling results<sup>24</sup>, which indicates the produced  $\text{O}_2$  molecules are from water oxidation rather than lattice oxygen oxidation. As a control sample, we performed another SSW-NN on  $\text{Ni}_{0.75}\text{Fe}_{0.25}\text{O}_y\text{H}_z\cdot\text{mH}_2\text{O}$ , where the stoichiometry of lattice oxygen is fixed at  $y=2$  and no lattice oxygen coupling is allowed to occur. Our calculations show that the searched GM structure,  $\text{Ni}_{0.75}\text{Fe}_{0.25}\text{O}_2\text{H}$ , comprises alternated  $\text{Ni}(\text{OH})_2$  and  $\text{Ni}_{0.5}\text{Fe}_{0.5}\text{O}_2$  sheets with no  $\text{H}_2\text{O}$  molecules in the interlayer space (Supplementary Fig. 22). OER proceeds via a lattice-oxygen-mediated mechanism (LOM) on  $\text{Ni}_{0.75}\text{Fe}_{0.25}\text{O}_2\text{H}$  (010) surface, *i.e.*,  $^*\text{O}_{\text{latt}} + ^*\text{H}_2\text{O} \rightarrow ^*\text{O}_{\text{latt}} + ^*\text{OH} \rightarrow ^*\text{O}_{\text{latt}} + ^*\text{O} \rightarrow ^*\text{O}-\text{O}_{\text{latt}} \rightarrow ^*\text{?} + \text{O}_2(\text{g}) \rightarrow ^*\text{O}_{\text{latt}}\text{H} \rightarrow ^*\text{O}_{\text{latt}} + ^*\text{H}_2\text{O}$ . The detailed comparisons of AEM and LOM on both surfaces can be seen in Supplementary Figs. 23 and 24.

We compared the kinetic barriers of OER on  $\text{Ni}_{0.75}\text{Fe}_{0.25}\text{O}_3\text{H}_{0.5}\cdot\text{H}_2\text{O}$  (010) and  $\text{Ni}_{0.75}\text{Fe}_{0.25}\text{O}_2\text{H}$  (010) surfaces at 1.53  $V_{\text{RHE}}$ . The rate-determining step (*r.d.s*) on  $\text{Ni}_{0.75}\text{Fe}_{0.25}\text{O}_3\text{H}_{0.5}\cdot\text{H}_2\text{O}$  (010) is that the nucleophilic  $\text{OH}^-$  attacks the terminal  $\text{Fe}=\text{O}$  intermediate to form  $\text{Fe}-\text{OOH}$  ( $\text{O03} \rightarrow \text{TS1} \rightarrow \text{O05}$ ), which has a low energy barrier of 0.34 eV. However, for  $\text{Ni}_{0.75}\text{Fe}_{0.25}\text{O}_2\text{H}$  (010), the *r.d.s* is oxygen coupling to form a  $\text{Fe}-(\eta^2-\text{O}_2)$  intermediate ( $\text{O2} \rightarrow \text{TS2} \rightarrow \text{O4}$ ) with a high energy barrier of 0.63 eV. Thus, the energy barrier on  $\text{Ni}_{0.75}\text{Fe}_{0.25}\text{O}_3\text{H}_{0.5}\cdot\text{H}_2\text{O}$  is 0.29 eV lower than that on  $\text{Ni}_{0.75}\text{Fe}_{0.25}\text{O}_2\text{H}$ . We have also checked the energetic profiles on two surfaces by using HSE06 and HSE06 with  $\alpha = 0.15$ , as shown in Supplementary Figs. 25 and 26. All results confirm that  $\text{Ni}_{0.75}\text{Fe}_{0.25}\text{O}_3\text{H}_{0.5}\cdot\text{H}_2\text{O}$  with  $\text{O}_{\text{latt}}-\text{O}_{\text{latt}}$  is more active than  $\text{Ni}_{0.75}\text{Fe}_{0.25}\text{O}_2\text{H}$ . Therefore, the  $\text{O}_{\text{latt}}-\text{O}_{\text{latt}}$  ligands can benefit OER on its nearby Fe sites.

To further understand  $\text{O}_{\text{latt}}-\text{O}_{\text{latt}}$  triggered Fe-activation from an atomic view, we compared the bonding strength of  $\text{Fe}-\text{OH}$  on two structures, which is the key of faster OER kinetics according to the Sabatier principle<sup>24</sup>. The bond length of  $\text{Fe}-\text{OH}$  in  $\text{Ni}_{0.75}\text{Fe}_{0.25}\text{O}_3\text{H}_{0.5}\cdot\text{H}_2\text{O}$ , 1.841 Å, is longer than that in  $\text{Ni}_{0.75}\text{Fe}_{0.25}\text{O}_2\text{H}$ , 1.828 Å (Supplementary Fig. 27), indicative of a weaker bonding strength of  $\text{Fe}-\text{OH}$  with the presence of  $\text{O}_{\text{latt}}-\text{O}_{\text{latt}}$ . To provide a deep insight into the dissimilar bonding strength between two surfaces, we further analyzed their electronic structures. The on-site spins of surface Fe are 3.79 and 3.39  $\mu\text{B}$  for  $\text{Ni}_{0.75}\text{Fe}_{0.25}\text{O}_3\text{H}_{0.5}\cdot\text{H}_2\text{O}$  and  $\text{Ni}_{0.75}\text{Fe}_{0.25}\text{O}_2\text{H}$ , respectively (Fig. 4a and Supplementary Fig. 22). According to the ligand field theory, the on-site spin represents the oxidation state (OS) of Fe (*e.g.*,  $\text{Fe}^{3+}$  is  $\sim 5 \mu\text{B}$ ), and the dissimilar on-site spins indicate the OS of Fe in  $\text{Ni}_{0.75}\text{Fe}_{0.25}\text{O}_3\text{H}_{0.5}\cdot\text{H}_2\text{O}$  surface is lower than that in  $\text{Ni}_{0.75}\text{Fe}_{0.25}\text{O}_2\text{H}$ . Consistently, the PDOS of Fe in  $\text{Ni}_{0.75}\text{Fe}_{0.25}\text{O}_3\text{H}_{0.5}\cdot\text{H}_2\text{O}$  surface shows a lower band center (-5.76 eV vs. Fermi level) than that in  $\text{Ni}_{0.75}\text{Fe}_{0.25}\text{O}_2\text{H}$  (-5.57 eV vs. Fermi level) (Supplementary Fig. 28). The lower OS of Fe in  $\text{Ni}_{0.75}\text{Fe}_{0.25}\text{O}_3\text{H}_{0.5}\cdot\text{H}_2\text{O}$  can be attributed to the oxidation of adjacent  $\text{O}_{\text{latt}}-\text{O}_{\text{latt}}$  to superoxides, evidenced by the on-site spins of 0.36-0.61  $\mu\text{B}$  (see O02 step in Fig. 4a). The lower Fe OS of  $\text{Ni}_{0.75}\text{Fe}_{0.25}\text{O}_3\text{H}_{0.5}\cdot\text{H}_2\text{O}$  implies that the Fe has more electrons in the  $e_g$  orbital, an anti-bonding state of the  $\text{Fe}-\text{OH}$ , which leads to a weaker  $\text{Fe}-\text{OH}$  bond. Therefore, the Fe OS can well explain the diminished bonding strength of  $\text{Fe}-\text{OH}$  after  $\text{O}_{\text{latt}}-\text{O}_{\text{latt}}$  formation, which is the key of enhanced OER activity.

## Conclusion

The key role of  $O_{\text{latt}}-O_{\text{latt}}$  ligands for Fe activation is demonstrated in Fe-based TM oxides/hydroxides, the state-of-the-art OER electrocatalysts in alkaline. We revealed an *in-situ* phase evolution and formation of  $O_{\text{latt}}-O_{\text{latt}}$  ligands in  $Ni_{1-x}Fe_xO_yH_z$ , and further discovered a  $O_{\text{latt}}-O_{\text{latt}}$  triggered Fe activation in TM oxides/hydroxides with different electronic and geometry structures. Mechanistic study indicates that  $O_{\text{latt}}-O_{\text{latt}}$  ligands induced a local coordination restructuring of Fe sites and diminished Fe–OH bonds, which is the key to improve OER. To conclude, our work establishes a new paradigm showing the importance of ligands restructuring on activating the metal centers in electrocatalysis. Broadly, these findings can provide potential guidance for the future development of more technically relevant oxygen-redox materials, such as for anodic electrocatalysis and lithium-ion batteries.

## References

1. Jiao, Y., Zheng, Y., Jaroniec, M. & Qiao, S. Z. Design of electrocatalysts for oxygen- and hydrogen-involving energy conversion reactions. *Chem. Soc. Rev.* **44**, 2060-2086 (2015).
2. Seh, Z. W. *et al.* Combining theory and experiment in electrocatalysis: Insights into materials design. *Science* **355**, eaad4998 (2017).
3. Gür, T. M. Review of electrical energy storage technologies, materials and systems: challenges and prospects for large-scale grid storage. *Energy Environ. Sci.* **11**, 2696-2767 (2018)
4. Kibsgaard, J. & Chorkendorff, I. Considerations for the scaling-up of water splitting catalysts. *Nat. Energy* **4**, 430-433 (2019).
5. Bockris, O.J. & Otagawa, T. The electrocatalysis of oxygen evolution on perovskites. *J. Electrochem. Soc.* **131**, 290-302 (1984).
6. Suntivich, J., May, K. J., Gasteiger, H. A., Goodenough, J. B. & Shao-Horn, Y. A perovskite oxide optimized for oxygen evolution catalysis from molecular orbital principles. *Science* **334**, 1383-1385 (2011).
7. Sun, Y. *et al.* Covalency competition dominates the water oxidation structure–activity relationship on spinel oxides. *Nat. Catal.* **3**, 554-563 (2020).
8. Subbaraman, R., Tripkovic, D., Chang, KC. *et al.* Trends in activity for the water electrolyser reactions on 3d M(Ni,Co,Fe,Mn) hydr(oxy)oxide catalysts. *Nat. Mater.* **11**, 550-557 (2012).
9. Burke, M. S., Enman, L. J., Batchellor, A. S., Zou, S. & Boettcher, S. W. Oxygen evolution reaction electrocatalysis on transition metal oxides and (oxy)hydroxides: activity trends and design principles. *Chem. Mater.* **27**, 7549-7558 (2015).
10. Chung, D. Y. *et al.* Dynamic stability of active sites in hydr(oxy)oxides for the oxygen evolution reaction. *Nat. Energy* **5**, 222-230 (2020).
11. Yeo, B. S. & Bell, A. T. Enhanced activity of gold-supported cobalt oxide for the electrochemical evolution of oxygen. *J. Am. Chem. Soc.* **133**, 5587-5593 (2011).

12. Chen, J. Y. *et al.* Operando analysis of NiFe and Fe oxyhydroxide electrocatalysts for water oxidation: Detection of Fe<sup>4+</sup> by Mossbauer spectroscopy. *J. Am. Chem. Soc.* **137**, 15090-15093 (2015).
13. Zheng, X. *et al.* Theory-driven design of high-valence metal sites for water oxidation confirmed using in situ soft X-ray absorption. *Nat. Chem.* **10**, 149-154 (2018).
14. Mefford, J. T. *et al.* Correlative operando microscopy of oxygen evolution electrocatalysts. *Nature* **593**, 67-73 (2021).
15. Grimaud, A. *et al.* Activating lattice oxygen redox reactions in metal oxides to catalyse oxygen evolution. *Nat. Chem.* **9**, 457-465 (2017).
16. Anderson, J. S., Rittle, J. & Peters, J. C. Catalytic conversion of nitrogen to ammonia by an iron model complex. *Nature* **501**, 84-87 (2013).
17. Čorić, I. *et al.* Binding of dinitrogen to an iron-sulfur-carbon site. *Nature* **526**, 96-99 (2015).
18. Grimaud, A., Diaz-Morales, O., Han, B. *et al.* Activating lattice oxygen redox reactions in metal oxides to catalyse oxygen evolution. *Nat. Chem* **9**, 457–465 (2017).
19. Grimaud, A. *et al.* Activation of surface oxygen sites on an iridium-based model catalyst for the oxygen evolution reaction. *Nat. Energy* **2**, 16189 (2017).
20. Huang, Z. F. *et al.* Chemical and structural origin of lattice oxygen oxidation in Co–Zn oxyhydroxide oxygen evolution electrocatalysts. *Nat. Energy* **4**, 329-338 (2019).
21. Nong, H.N., Falling, L.J., Bergmann, A. *et al.* Key role of chemistry versus bias in electrocatalytic oxygen evolution. *Nature* **587**, 408-413 (2020).
22. Lin, C., Li, J.L., Li, X. *et al.* In-situ reconstructed Ru atom array on  $\alpha$ -MnO<sub>2</sub> with enhanced performance for acidic water oxidation. *Nat. Catal* **4**, 1012–1023 (2021).
23. Corrigan, D. A. The catalysis of the oxygen evolution reaction by Iron impurities in thin film Nickel oxide electrodes. *J. Electrochem. Soc.* **134**, 377-384 (1987).
24. Roy, C. *et al.* Impact of nanoparticle size and lattice oxygen on water oxidation on NiFeOxHy. *Nat. Catal.* **1**, 820-829 (2018).
25. Louie, M. W. & Bell, A. T. An investigation of thin-film Ni-Fe oxide catalysts for the electrochemical evolution of oxygen. *J. Am. Chem. Soc.* **135**, 12329-12337 (2013).
26. Trotochaud, L., Young, S. L., Ranney, J. K. & Boettcher, S. W. Nickel-iron oxyhydroxide oxygen-evolution electrocatalysts: The role of intentional and incidental iron incorporation. *J. Am. Chem. Soc.* **136**, 6744-6753 (2014).
27. Friebel, D. *et al.* Identification of highly active Fe sites in (Ni,Fe)OOH for electrocatalytic water splitting. *J. Am. Chem. Soc.* **137**, 1305-1313 (2015).
28. Ahn, H. S. & Bard, A. J. Surface interrogation scanning electrochemical microscopy of Ni<sub>1-x</sub>Fe<sub>x</sub>OOH (0 < x < 0.27) oxygen evolving catalyst: Kinetics of the "fast" Iron sites. *J. Am. Chem. Soc.* **138**, 313-318 (2016).
29. Stevens, M. B., Trang, C. D. M., Enman, L. J., Deng, J. & Boettcher, S. W. Reactive Fe-sites in Ni/Fe (Oxy)hydroxide are responsible for exceptional oxygen electrocatalysis activity. *J. Am. Chem. Soc.*

- 139, 11361-11364 (2017).
30. Lee, S., Banjac, K., Lingenfelder, M. & Hu, X. Oxygen isotope labeling experiments reveal different reaction sites for the oxygen evolution reaction on Nickel and Nickel Iron oxides. *Angew. Chem. Int. Ed.* **58**, 10295-10299 (2019).
31. Dionigi, F. *et al.* In-situ structure and catalytic mechanism of NiFe and CoFe layered double hydroxides during oxygen evolution. *Nat. Commun.* **11**, 2522 (2020).
32. Hao, Y. *et al.* Recognition of Surface Oxygen Intermediates on NiFe Oxyhydroxide Oxygen-Evolving Catalysts by Homogeneous Oxidation Reactivity. *J. Am. Chem. Soc.* **143**, 1493-1502 (2021).
33. Kuai, C., Xu, Z., Xi, C. *et al.* Phase segregation reversibility in mixed-metal hydroxide water oxidation catalysts. *Nat. Catal.* **3**, 743–753 (2020).
34. Diaz-Morales, O., Ferrus-Suspedra, D. & Koper, M. T. M. The importance of nickel oxyhydroxide deprotonation on its activity towards electrochemical water oxidation. *Chem. Sci.* **7**, 2639-2645 (2016).
35. Cramer, C. J., Tolman, W. B., Theopold, K. H. & Rheingold, A. L. Variable character of O–O and M–O bonding in side-on ( $\eta^2$ ) 1:1 metal complexes of O<sub>2</sub>. *Proc. Natl Acad. Sci. USA* **100**, 3635–3640 (2003).
36. Cho, J., Sarangi, R. & Nam, W. Mononuclear metal–O<sub>2</sub> complexes bearing macrocyclic N-tetramethylated cyclam ligands. *Acc. Chem. Res.* **45**, 1321–1330 (2012).
37. Zhang, S. *et al.* Evidence of matrix lattice distortion in Zn<sub>1-x</sub>Co<sub>x</sub>O nanocrystals. *J. Phys. Chem. C* **113**, 4263-4269 (2009).
38. Han, Y. *et al.* Preparation of Ni<sup>2+</sup>–Fe<sup>3+</sup> layered double hydroxide material with high crystallinity and well-defined hexagonal shapes. *Chem. Mater.* **20**, 360-363 (2008).
39. Tong, Y. *et al.* Vibronic superexchange in double perovskite electrocatalyst for efficient electrocatalytic oxygen evolution. *J. Am. Chem. Soc.* **140**, 11165-11169 (2018).

## Methods

### Material synthesis.

**Synthesis of Ni<sub>1-x</sub>Fe<sub>x</sub>O<sub>y</sub>H<sub>z</sub>.** Ni<sub>1-x</sub>Fe<sub>x</sub>O<sub>y</sub>H<sub>z</sub> was synthesized via a modified hydrothermal procedure<sup>38</sup>. Desired ratios of Ni and Fe were obtained by mixing different stoichiometries of Ni(NO<sub>3</sub>)<sub>2</sub> and Fe(NO<sub>3</sub>)<sub>3</sub>·9H<sub>2</sub>O in 50 mL deionized water to reach a total concentration of 20 mM. 35 mM urea was added into the solution to assist hydrolysis. Then, trisodium citrate (0.25 mM) was added into the above solution under stirring. All chemicals were used as purchased. After thoroughly mixing, the solution was sealed in a Teflon-lined stainless-steel autoclave and hydrothermally treated at 150 °C for 48 h. The obtained powder was washed by deionized water for two times and ethanol for one time, and finally dried at 50 °C under air condition.

**Synthesis of  $\text{LaNi}_{1-x}\text{Fe}_x\text{O}_3$ .**  $\text{LaNi}_{1-x}\text{Fe}_x\text{O}_3$  was synthesized via a sol-gel method<sup>39</sup>. Desired ratios of La, Ni and Fe were obtained by mixing different stoichiometries of  $\text{La}(\text{NO}_3)_3 \cdot 9\text{H}_2\text{O}$ ,  $\text{Ni}(\text{NO}_3)_2$  and  $\text{Fe}(\text{NO}_3)_3 \cdot 9\text{H}_2\text{O}$  in 20 mL deionized water. Then, citric acid and acrylamide were added into the above solution under stirring. The molar ratio of total metal ions, citric acid and acrylamide was controlled to be 1:3:9. After thoroughly stirring, the mixture was heated to 110 °C to generate gel, which was subsequently dried in air at 150 °C for 12 h. Finally, after calcination at 800 °C for 6 h, the  $\text{LaNi}_{1-x}\text{Fe}_x\text{O}_3$  powder with different Ni/Fe stoichiometries were obtained.

**Synthesis of  $\text{NiFe}_2\text{O}_4$ .**  $\text{NiFe}_2\text{O}_4$  was synthesized via a similar method as  $\text{LaNi}_{1-x}\text{Fe}_x\text{O}_3$ .  $\text{Ni}(\text{NO}_3)_2$  and  $\text{Fe}(\text{NO}_3)_3 \cdot 9\text{H}_2\text{O}$  (molar Ni: Fe=1:2) were dissolved in 20 mL of deionized water. Then, citric acid and acrylamide were added into the above solution under stirring. The molar ratio of total metal ions, citric acid and acrylamide was controlled to be 1:3:9. After thoroughly stirring, the mixture was heated to 110 °C to generate gel. The obtained gel was dried in air at 150 °C for 12 h. Finally, after calcination at 800 °C for 6 h, the  $\text{NiFe}_2\text{O}_4$  powder was obtained.

**Synthesis of ultra-thin  $\text{MFeO}_x\text{H}_y$ .** Ultra-thin  $\text{MFeO}_x\text{H}_y$  (M= Mn, Fe, Co, Ni and Cu) were synthesized using formamide as an inhibitor of layer growth<sup>30,40</sup>, in order to fully expose the lattice oxygen and ensure the total exchange of  $^{16}\text{O}$  by isotope labelled  $^{18}\text{O}$  in solution. Typically, a 10.0 mL nitrate solution containing 37.5 mM of total metal ions (molar M:Fe=3:1) was mixed with 20.0 mL of 10 mM  $\text{NaNO}_3$  containing 23 vol% formamide. Under stirring, the solution was heated up to 80 °C. Then, the pH of solution was adjusted to ~10 by dropping 0.25 M KOH. After cooling down to the room temperature, the product was washed with ethanol and deionized water (1:1 vol%) for three times. Finally, the obtained ultra-thin  $\text{MFeO}_x\text{H}_y$  was dispersed and stored in deionized water.

## Characterizations.

### Off-line physical characterizations.

The XRD patterns were recorded on a Bruker D8 Advance diffractometer with Cu Ka radiation ( $\lambda = 1.5418 \text{ \AA}$ ) and a Lynx Eye detector. The specific surface area was determined by BET  $\text{N}_2$  adsorption isotherms on an ASAP Tristar II 3020 after 20 h outgassing at 80 °C. The  $\text{N}_2$  adsorption was measured at 77 K in a relative pressure range  $p/p_0$  of 0.05-0.3. The ICP-OES tests were performed on Thermo Fisher Scientific iCAP 7400.

### OER electrochemical measurements.

The electrochemical measurement was performed using a Biologic VSP-300 potentiostat. All CV tests were measured using a rotation disk electrode (RDE) with 1600 rpm using a PINE MSR rotator in a 1 M purified Fe free-KOH aqueous solution (the purification procedure was rigorously following a previously reported method<sup>26</sup>). All catalysts were loaded on glassy carbon electrodes (as working electrodes) and mixed with a certain amount of carbon black to ensure the conductivity. A platinum wire

and Hg/HgO (CHI instruments) were used as the counter and reference electrode, respectively. The potential of Hg/HgO was routinely calibrated against a reversible hydrogen electrode (RHE, eDAQ Inc.). All potentials in electrochemical tests were converted to the RHE scale with resistance compensation, which was determined by electrochemical impedance measurement.

The catalyst inks were prepared by mixing 2 mg of the catalyst, 2 mL deionized water, 2 mL ethanol, 0.6 mg carbon black and 20  $\mu\text{L}$  Nafion (5 wt %). All inks were ultrasonicated for at least 30 min to ensure the dispersity. Then, 20  $\mu\text{L}$  of the as-prepared ink was dropped onto a glassy carbon electrode (0.196  $\text{cm}^2$ ) and dried in air naturally. The mass loading of catalyst for OER test is calculated to be  $\sim 51 \mu\text{g}/\text{cm}_{\text{geo}}^2$ .

### ***Operando* Raman measurement.**

All Raman spectra were recorded by a Horiba JY XploRA Raman spectrometer under a 638 nm laser excitation. The Raman shift was calibrated using the silicon peak at  $521 \text{ cm}^{-1}$  before measurements. We customized a three-electrode cell to probe the structural evolution of catalysts (see the schematic illustration in Supplementary Fig. 29). Catalysts were loaded on an electrochemically roughened Au electrode to obtain the surface-enhanced Raman signal (SERS)<sup>41</sup>. To prepare a SERS substrate, 10 nm Ti/100 nm Au electrode was thermally evaporated onto a silicon substrate. The roughened Au can be obtained by  $\sim 20$  oxidation-reduction CV cycles between  $-0.3 \text{ V}$  (30 s hold) and  $1.3 \text{ V}$  (1.3 s hold) vs. Ag/AgCl in a 0.1 M KCl aqueous solution<sup>30</sup>.

### ***Operando* XANES and EXAFS measurement.**

The XAS measurements were carried out at BL11B beamline of Shanghai Synchrotron Radiation Facility (SSRF). For all XAS tests, monochromatized X-ray beam was provided by a double-crystal Si (111) monochromator, and the photon energies were calibrated to the first inflection point of the K-edge from Ni foil at 8333 eV and Fe foil at 7112 eV, respectively. The reference spectra were recorded in a transmission mode, while all the spectra of catalysts were measured in a fluorescence mode with a Lytle detector filled with Argon gas. All *operando* measurements were carried out in a three-electrode cell (see Supplementary Fig. 30). The catalysts were loaded on a carbon paper ( $\sim 1 \text{ mg}/\text{cm}^2$ ) as the working electrode. A platinum wire and Hg/HgO were used as the counter and reference electrode, respectively, and the electrolyte was 1 M purified KOH. Ni K-edge spectra was recorded from 8133 eV to 9128 eV and Fe K-edge in the range of 6912 eV to 7912 eV. The data collected were normalized and processed in the ATHENA program integrated with IFEFFIT software package.

### **Data analysis.**

#### **EXAFS analysis and fittings.**

The acquired EXAFS data were processed according to standard procedures using the ATHENA module implemented in the IFEFFIT software packages<sup>42</sup>. The  $k^3$ -weighted EXAFS spectra were obtained by subtracting the post-edge background from the overall absorption and then normalizing with respect to

the edge-jump step. Subsequently,  $k^3$ -weighted  $\chi(k)$  data of Ni K-edge and Fe K-edge were Fourier transformed to real (R) space using a hanning windows ( $dk = 1.0 \text{ \AA}^{-1}$ ) to separate the EXAFS contributions from different coordination shells.

To obtain the quantitative structural parameters around central atoms, least-squares curve parameter fitting was performed using the ARTEMIS module of IFEFFIT software packages<sup>42</sup>, which is based on the following equation:

$$\chi(k) = S_0^2 \sum_j \frac{N_j}{kR_j^2} f_{eff_j}(\pi, k, R_j) e^{-2\sigma_j^2 k^2} e^{-2R_j/\lambda_j(k)} \sin(2kR_j + \phi_{ij}(k))$$

$N_j$  denotes the number of neighboring atoms in  $j^{\text{th}}$  shell at a distance of  $R_j$  from the central atom.  $S_0^2$  is an amplitude reduction factor.  $f_{eff_j}(\pi, k, R_j)$  is the effective curved-wave backscattering amplitude.  $R_j$  is the distance between the X-ray absorbing central atom and the atoms in the  $j^{\text{th}}$  atomic shell.  $\sigma_j^2$  is the Debye-Waller parameter of the  $j^{\text{th}}$  atomic shell.  $\lambda_j(k)$  is the electron mean free path.  $\phi_{ij}(k)$  is the ab initio phase function for shell  $j^{\text{th}}$ .

For as-synthesized  $\text{Ni}_{0.63}\text{Fe}_{0.37}\text{O}_x\text{H}_y$ ,  $\text{LaNi}_{0.61}\text{Fe}_{0.39}\text{O}_3$  and  $\text{NiFe}_2\text{O}_4$ , both M–O and M–M shells were fitted to distinguish local structures of hydroxide, perovskite and spinel. The coordination numbers (CN) were fixed as the nominal values and K range used for the simulations were  $2.5\text{-}12 \text{ \AA}^{-1}$ . For *operando* XAS, only M–O shell was fitted to monitor M–O local structure change during electrooxidation process.  $S_0^2$  was fixed to 0.70. The K range used in *operando* data fitting was  $2.5\text{-}10.5 \text{ \AA}^{-1}$  to exclude the noise in high K range. All fitting results are listed in Supplementary Fig. 31, Tables 3 and 6-8.

### TOF calculation.

The  $\text{TOF}_{\text{Fe}}$  (assuming all Fe ions are active sites) was calculated by the following equation:

$$\text{TOF}_{\text{Fe}} = \frac{r_{\text{O}_2}}{N_{\text{Fe}}} = \frac{i \times N_A}{4 \times F \times N_{\text{Fe}}}$$

Where  $i$ ,  $N_A$ ,  $F$  and  $N_{\text{Fe}}$  represent the current (A) at an overpotential of 300 mV, Avogadro number ( $6.022 \times 10^{23}$  O<sub>2</sub> molecules per mol O<sub>2</sub>), Faraday constant (96,485 C/mol) and the number of all Fe in catalysts, respectively.

The  $\text{TOF}_{\text{surface-Fe}}$  (assuming Fe ions locating at surface are active) was calculated by the following equation:

$$\text{TOF}_{\text{surface-Fe}} = \frac{r_{\text{O}_2}}{N_{\text{surface-Fe}}} = \frac{i \times N_A}{4 \times F \times N_{\text{surface-Fe}}}$$

To determine the number of surface Fe ions ( $N_{\text{surface-Fe}}$ ), we calculated the surface density of 3d metal atoms ( $\rho$ ) of three structures based on their atomic arrangements, and either XAS or XRD data (see Supplementary Note 2 and Fig. 32). Therefore, we calculated  $N_{\text{surface-Fe}}$  by the following equation:

$$N_{\text{surface-Fe}} = S \times \rho \times \text{Fe atom\%}$$

Where S and Fe atom% represent the surface area determined by BET (see Supplementary Fig. 33 and Table 9) and Fe content in 3d metal atoms. This approach was regarded as a reasonable way to evaluate the intrinsic activities of powdery catalysts as previously reported<sup>43,44</sup>.

## Computational Methods.

### SSW-NN Simulation.

The stochastic surface walking is based on the global neural network potential (SSW-NN) method, as implemented in LASP code (<http://www.lasphub.com>)<sup>45,46</sup>, in which the SSW-NN achieves fast global potential energy surface (PES) exploration to resolve the stable phase of Ni-Fe *superoxo*-hydroxide during the reaction. The Fe-Ni-O-H quaternary element G-NN potential was developed by self-learning the DFT global PES data set, which was generated from the SSW global PES exploration for systems with different Fe-Ni-O-H compositions or structures (see Supplementary Note 3 and Table 11). There are six steps: (1) Generating the global dataset from the SSW global optimization trajectories and computing the dataset using DFT calculation; (2) Training the NN potential with dataset; (3) Benchmarking the accuracy between the current NN potential and DFT calculation for selected structures from SSW trajectories and retraining the NN potential by adding new dataset; (4) Iteratively performing (1–3) steps until the PES deviation is low enough. The accuracy of G-NN potential is typically 5-10 meV/atom for RMSE of energy and 0.1-0.2 eV/Å for RMSE of force; (5) Performing the SSW global optimization on the NN PES for target problem. (6) Recomputing the energy of key structures with DFT calculations. Zero-point energy (ZPE) was calculated from the phono spectra using the density functional perturbation theory to obtain the convex hull diagram.

### DFT Calculations.

All DFT calculations were performed using Vienna *Ab initio* Simulation Package (VASP)<sup>47</sup> with projected augmented wave (PAW) pseudo-potentials and the Perdew-Burke-Ernzerhof (PBE) functional with Hubbard term correction<sup>48,49</sup>. The effective Hubbard term ( $U_{\text{eff}}$ ) was set at 3.3 eV for Fe and 5.5 eV for Ni in accordance with the linear response approach<sup>50,51</sup>. The plane-wave cutoff energy was set to 500 eV. The Monkhorst-Pack scheme with k-point meshes of (2×4×2) and (2×4×1) are utilized for bulk and slab

systems, respectively. The limited memory Broyden-Fletcher-Goldfarb-Shanno (LBFGS) method is used for geometry relaxation until the maximal force is less than 0.08 eV/Å. The composition of surface with surface superoxide is Ni<sub>24</sub>Fe<sub>8</sub>O<sub>72</sub>H<sub>32</sub> in each unit cell with dimensions of 11.84×16.40 Å<sup>2</sup>. The solvation effect due to the long-range electrostatic interaction was modeled by a periodic continuum solvation model with modified Poisson-Boltzmann equation (CM-MPB)<sup>52,53</sup>. The computational hydrogen electrode (CHE) approach was utilized to evaluate the thermodynamics of OER on all Ni<sub>0.75</sub>Fe<sub>0.25</sub>O<sub>y</sub>H<sub>z</sub> surfaces. All the reported free energy changes in the OER refer to the electrode potential (U) at 1.53V<sub>RHE</sub>.

## Methods References

40. Yu, J., Martin, B. R., Clearfield, A., Luo, Z. & Sun, L. One-step direct synthesis of layered double hydroxide single-layer nanosheets. *Nanoscale***7**, 9448-9451 (2015).
41. Gao, P., Patterson, M. L., Tadayoni, M. A. & Weaver, M. J. Gold as a ubiquitous substrate for intense surface-enhanced Raman scattering. *Langmuir***1**, 173-176 (1985).
42. Ravel, B. & Newville, M. ATHENA, ARTEMIS, HEPHAESTUS: data analysis for X-ray absorption spectroscopy using IFEFFIT. *J. Synchrotron Rad.***12**, 537-541 (2005).
43. Wei, C. *et al.* Approaches for measuring the surface areas of metal oxide electrocatalysts for determining their intrinsic electrocatalytic activity. *Chem. Soc. Rev.***48**, 2518-2534 (2019).
44. Sun, Y. *et al.* Covalency competition dominates the water oxidation structure–activity relationship on spinel oxides. *Nat. Catal.***3**, 554-563 (2020).
45. Huang, S. D., Shang, C., Zhang, X. J. & Liu, Z. P. Material discovery by combining stochastic surface walking global optimization with a neural network. *Chem. Sci.***8**, 6327-6337 (2017).
46. Huang, S. D., Shang, C., Kang, P. L., Zhang, X. J. & Liu, Z. P. LASP: Fast global potential energy surface exploration. *WIREs Comput Mol Sci.***9**, e1415 (2019).
47. Kresse, G. & Furthmüller, J. Efficient iterative schemes for ab initio total-energy calculations using a plane-wave basis set. *Phys. Rev. B***54**, 11169-11186 (1996).
48. Perdew, J. P., Burke, K. & Ernzerhof, M. Generalized gradient approximation made simple. *Phys. Rev. Lett.***77**, 3865-3868 (1996).
49. Cococcioni, M. & de Gironcoli, S. Linear response approach to the calculation of the effective interaction parameters in the LDA + U method. *Phys. Rev. B***71**, 035105 (2005).
50. Li, Y. F. & Selloni, A. Mechanism and activity of water oxidation on selected surfaces of pure and Fe-doped NiO<sub>x</sub>. *ACS Catal.***4**, 1148-1153 (2014).

51. Li, Y. F. & Liu, Z. P. Structure and water oxidation activity of 3d metal oxides. *WIREs. Comput. Mol. Sci.***6**, 47-64 (2016).
52. Fattebert, J. L. & Gygi, F. Linear-scaling first-principles molecular dynamics with plane-waves accuracy. *Phys. Rev. B***73**, 115124 (2006).
53. Walter, M. G. *et al.* Solar water splitting cells. *Chem. Rev.***110**, 6446-6473 (2010).

## Declarations

**Acknowledgments.** This research was supported by National Natural Science Foundation of China (Grants 21872039, 21972023, 22072030 and 22022301), Science and Technology Commission of Shanghai Municipality (Grant 18JC1411700 and 19DZ2270100). We also thank the funding support from original personalized project of Fudan University.

**Author contributions.** L.Z. designed and conceived the experiment. G.S. fabricated the electrodes, performed the electrochemical and *in-situ* spectroscopy characterization. J.L., Z.L. and Y.L. carried out the DFT calculations. J.L and S.Z. helped on the XAS data analysis. All authors discussed the results and participated in writing the manuscript.

**Competing financial interests.** The authors declare no competing financial interests.

**Additional Information.** Additional Information accompanies this paper. Correspondence and requests for materials should be addressed to L.Z and Y.L.

## Figures

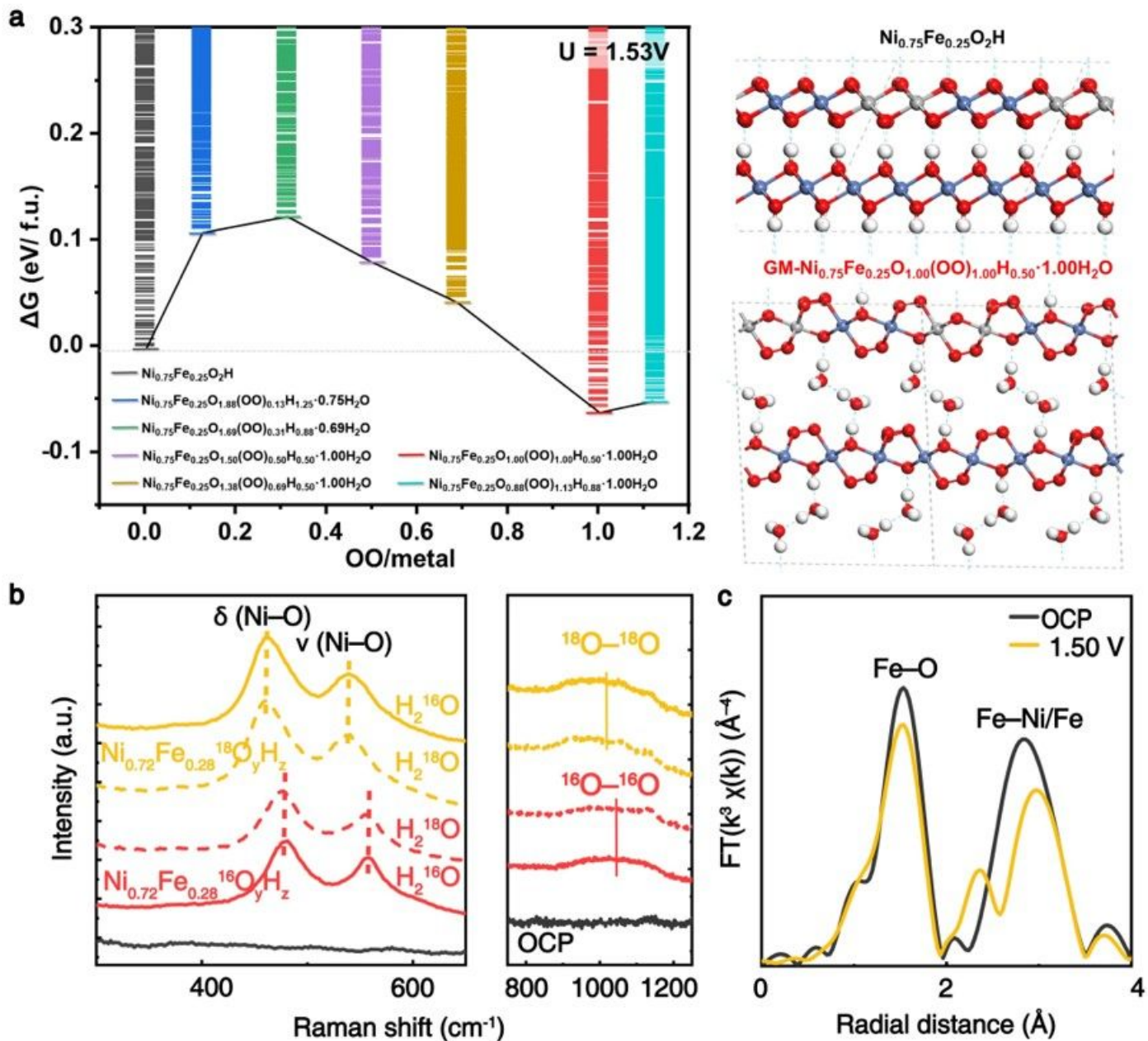


Figure 1

**$O_{latt}-O_{latt}$  formation under OER conditions.** **a**, The formation energy of  $Ni_{0.75}Fe_{0.25}O_xH_y \cdot zH_2O$  per f.u. The schematic illustration of GM structure without (top) and with (bottom)  $O_{latt}-O_{latt}$  ligands were shown on the right side. **b**, *Operando* electrochemical-Raman spectra of  $Ni_{0.72}Fe_{0.28}O_yH_z$  with isotope labelling. Solid red and yellow lines denote  $Ni_{0.72}Fe_{0.28}^{16}O_yH_z$  and  $Ni_{0.72}Fe_{0.28}^{18}O_yH_z$  in a purified  $^{16}O$ -KOH aqueous electrolyte at  $1.65 V_{RHE}$ , respectively, while dashed red and yellow lines denote  $Ni_{0.72}Fe_{0.28}^{16}O_yH_z$  and  $Ni_{0.72}Fe_{0.28}^{18}O_yH_z$  in a purified  $^{18}O$ -KOH aqueous electrolyte at  $1.65 V_{RHE}$ , respectively. **c**, *Operando* Fe K-edge FT-EXAFS of  $Ni_{0.63}Fe_{0.37}O_yH_z$ . All potentials were converted to the RHE scale.

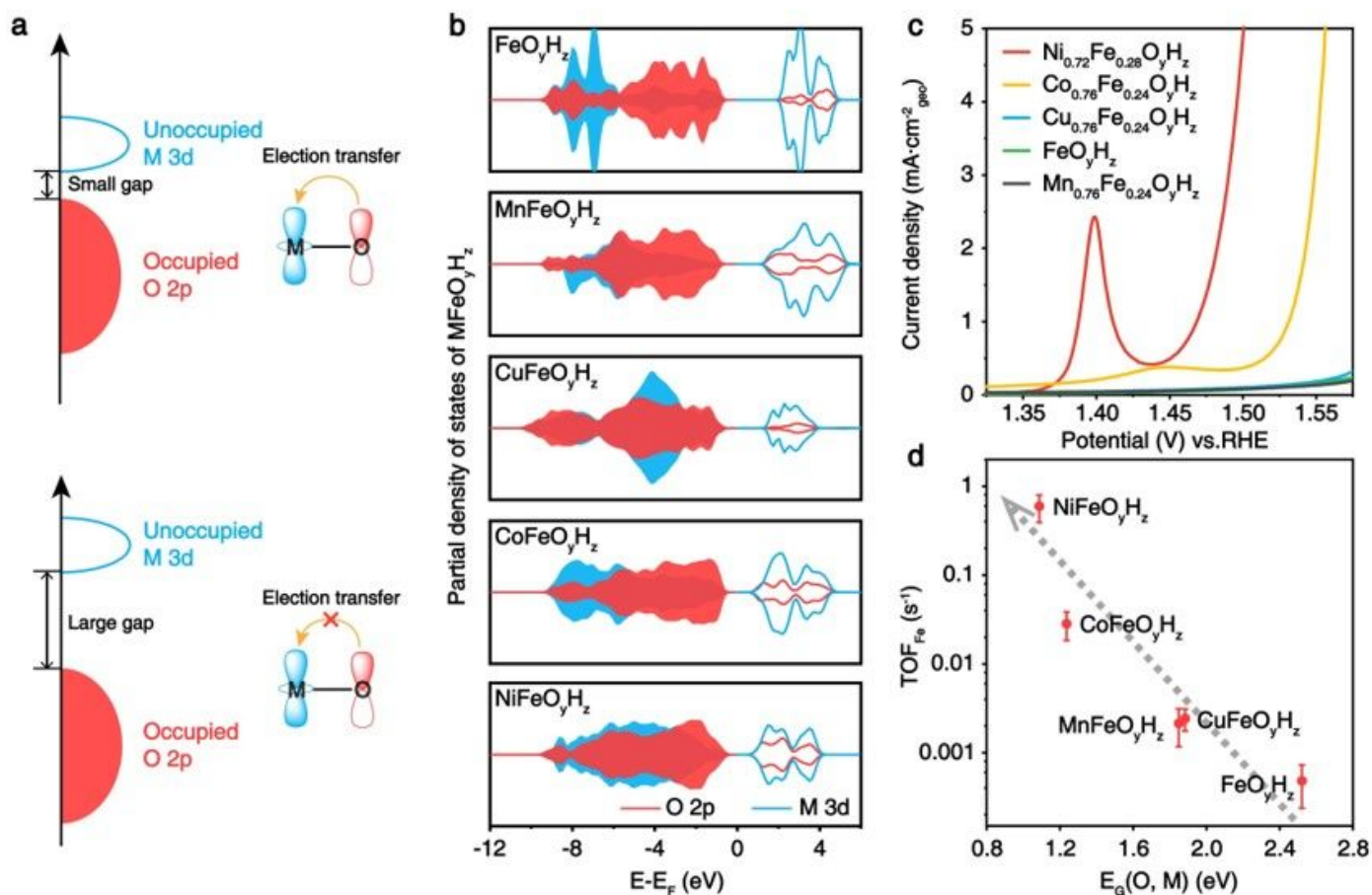


Figure 2

$\text{O}_{\text{latt}}-\text{O}_{\text{latt}}$  ligands triggered Fe activation in TM hydroxide. **a**, Band diagrams showing the electron transfer from O 2p to M 3d in TM oxides/hydroxides, where the  $3d_z^2$  orbital was used to represent unoccupied M 3d orbitals. **b**, PDOS of M 3d and O 2p in various  $\text{M}_{0.75}\text{Fe}_{0.25}\text{O}_y\text{H}_z$  (M=Mn, Fe, Co, Ni and Cu). **c**, Linear sweep voltammetry measurements of  $\text{M}_{1-x}\text{Fe}_x\text{O}_y\text{H}_z$  ( $x=0.25\pm 0.03$ ) with a 10 mV/s sweeping rate in a 1 M Fe-free KOH aqueous solution. **d**, Correlation between  $\text{TOF}_{\text{Fe}}$  and  $E_G(\text{O, M})$  in  $\text{M}_{1-x}\text{Fe}_x\text{O}_y\text{H}_z$  ( $x=0.25\pm 0.03$ ). For simplicity,  $\text{MFeO}_y\text{H}_z$  was used to denote the series of hydroxide in figures.

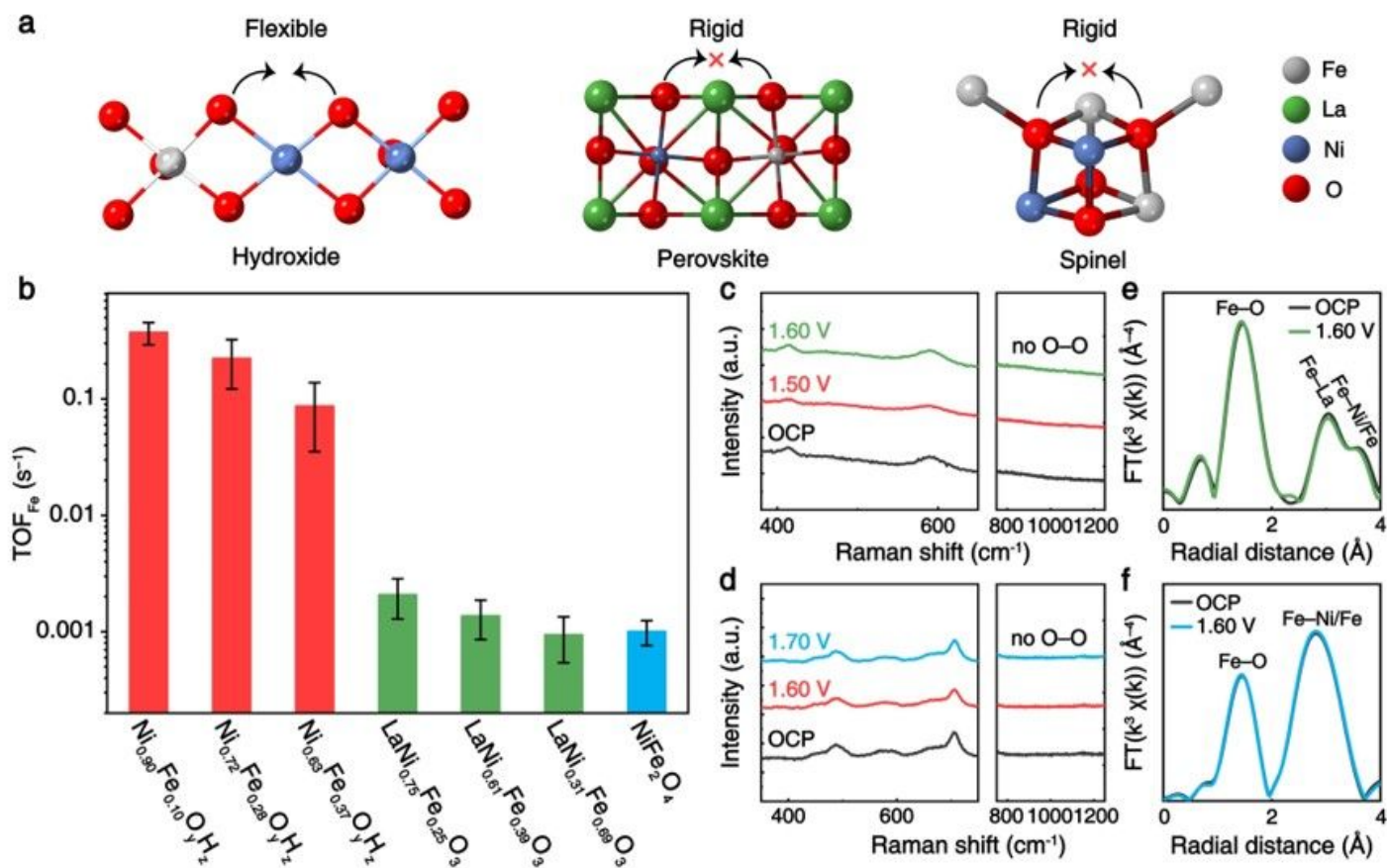


Figure 3

**O<sub>latt</sub>-O<sub>latt</sub> formation and Fe activation in different Fe-incorporated TM oxides/hydroxides.** **a**, The local geometric environments of lattice oxygen in hydroxide, perovskite and spinel. **b**, TOF<sub>Fe</sub> of Ni<sub>1-x</sub>Fe<sub>x</sub>O<sub>y</sub>H<sub>z</sub>, LaNi<sub>1-x</sub>Fe<sub>x</sub>O<sub>3</sub> and NiFe<sub>2</sub>O<sub>4</sub> at a 300 mV overpotential, assuming all Fe sites in catalysts are active. **c-d**, *Operando* electrochemical-Raman spectra of LaNi<sub>0.61</sub>Fe<sub>0.39</sub>O<sub>3</sub> (c) and NiFe<sub>2</sub>O<sub>4</sub> (d) under different applied potentials. **e-f**, *Operando* Fe K-edge FT-EXAFS of LaNi<sub>0.61</sub>Fe<sub>0.39</sub>O<sub>3</sub> (e) and NiFe<sub>2</sub>O<sub>4</sub> (f) under OCP and 1.60 V<sub>RHE</sub>. All potentials were converted to the RHE scale.

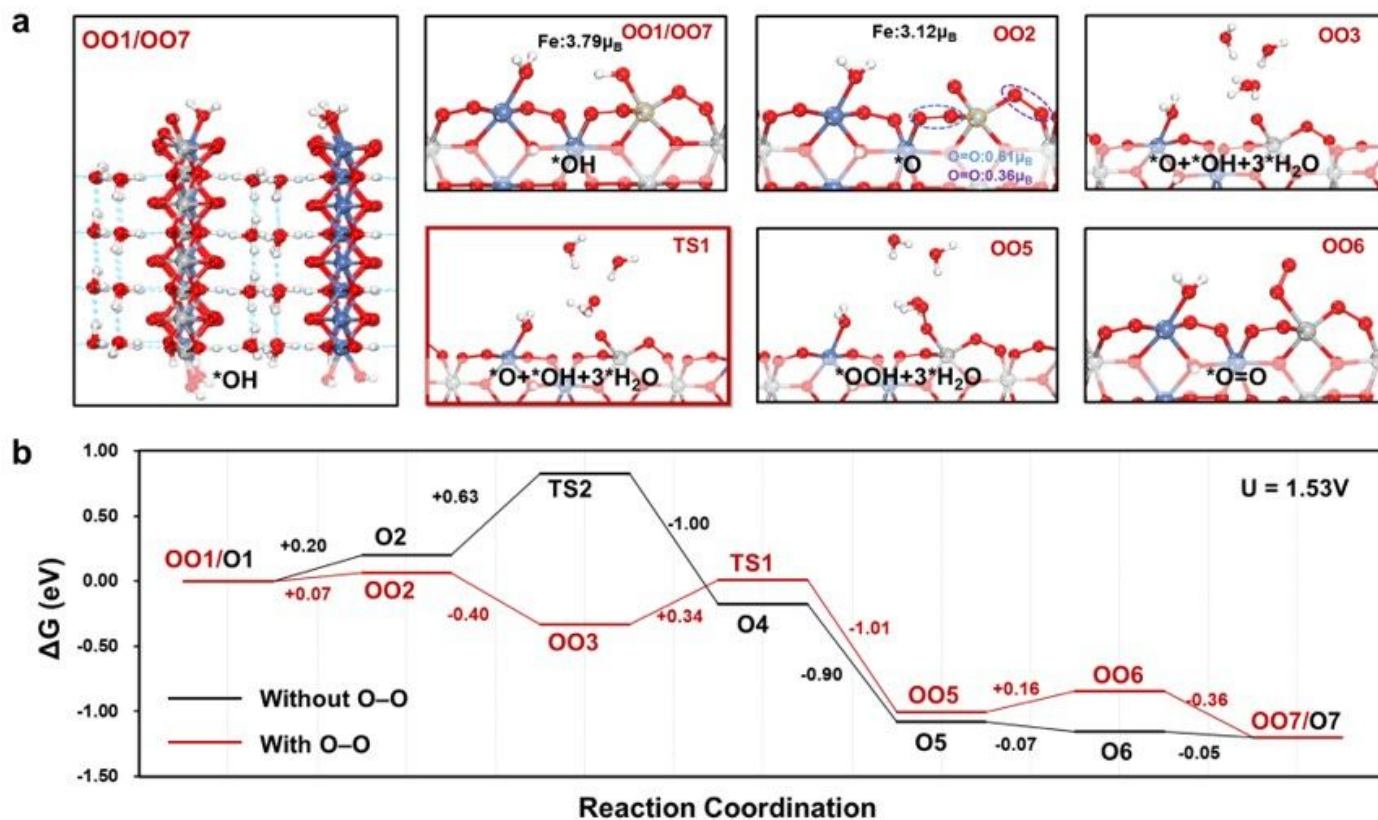


Figure 4

**Fe-activation mechanism at an atomic level.** **a**, The OER pathway on  $\text{Ni}_{0.75}\text{Fe}_{0.25}\text{O}_3\text{H}_{0.5}\cdot\text{H}_2\text{O}(010)$ . The *r.d.s* is the nucleophilic  $\text{OH}^-$  attacks the terminal  $\text{Fe}=\text{O}$  intermediate to form  $\text{Fe}-\text{OOH}$  ( $\text{OO3} \rightarrow \text{TS1} \rightarrow \text{OO5}$ ). **b**, The calculated free energy diagrams comparing  $\Delta\text{G}$  on Fe sites of  $\text{Ni}_{0.75}\text{Fe}_{0.25}\text{O}_3\text{H}_{0.5}\cdot\text{H}_2\text{O}$  (AEM) and  $\text{Ni}_{0.75}\text{Fe}_{0.25}\text{O}_2\text{H}$  (LOM) along OER pathways at  $1.53 V_{\text{RHE}}$ .

## Supplementary Files

This is a list of supplementary files associated with this preprint. Click to download.

- [SupplementaryData.docx](#)